

Instability of a thin viscous film flowing under an inclined substrate: the emergence and stability of rivulets

Pier Giuseppe Ledda^{1,†}, Gaétan Lerisson¹, Gioele Balestra²
and François Gallaire¹

¹Laboratory of Fluid Mechanics and Instabilities, École Polytechnique Fédérale de Lausanne, Lausanne CH-1015, Switzerland

²iPrint Institute, University of Applied Sciences and Arts of Western Switzerland, Fribourg CH-1700, Switzerland

(Received 4 August 2019; revised 31 July 2020; accepted 9 August 2020)

We study the pattern formation of a thin film flowing under an inclined planar substrate. The phenomenon is studied in the context of the Rayleigh–Taylor instability using the lubrication equation. Inspired by experimental observations, we numerically study the thin film response to a streamwise-invariant sinusoidal initial condition. The numerical response shows the emergence of predominant streamwise-aligned structures, modulated along the direction perpendicular to the flow, called rivulets. Oscillations of the thickness profile along the streamwise direction do not grow significantly when the inclination is very large or the liquid layer very thin. However, for small inclinations or thick films, streamwise perturbations grow on rivulets. A secondary stability analysis of one-dimensional and steady rivulets reveals a strong stabilization mechanism for large inclinations or very thin films. The theoretical results are compared with experimental measurements of the streamwise oscillations of the rivulet profile, showing a good agreement. The emergence of rivulets is investigated by studying the impulse response. Both the experimental observation and the numerical simulation show a marked anisotropy favouring streamwise-aligned structures. A weakly nonlinear model is proposed to rationalize the levelling of all but streamwise-aligned structures.

Key words: absolute/convective instability, nonlinear instability, thin films

1. Introduction

Coating flows are ubiquitous in nature and industrial applications. Nature provides astonishing examples of the capability of coating flows to modify the topography of the substrate via chemical and thermodynamic reactions. The structures that can be observed in limestone caves, known as *speleothems*, are characterized by a morphogenesis that is related to the hydrodynamic instability of a coating flow (Short *et al.* 2005; Meakin & Jamtveit 2010; Camporeale 2015; Bertagni & Camporeale 2017). These fascinating structures originate from the interaction between hydrodynamics and chemistry.

† Email address for correspondence: pier.ledda@epfl.ch

The control of the instability related to coating processes is an important task in industrial applications as many fabrication processes involve the presence of a thin film flowing on a substrate (Weinstein & Ruschak 2004). Thin elastic shells of constant thickness can be fabricated by polymerization of the film, as performed in Lee *et al.* (2016). Marthelot *et al.* (2018*b*) showed a remarkable example of control of the flow instability to produce textured surfaces, by rotation of a cylindrical substrate.

The Rayleigh–Taylor instability is a phenomenon that occurs when a heavier fluid is placed above a lighter one. When a horizontal flat interface is considered, under the only effect of gravity, all wavelengths are unstable (Rayleigh 1882; Taylor 1950). The introduction of capillary effects bounds the range of unstable wavelengths (Chandrasekhar 2013). When an upper wall confines the overhanging fluid, the resulting pattern is characterized by lenses arranged in hexagonal or square arrays (Fermigier *et al.* 1992). The lenses may saturate for small enough initial thickness (Marthelot *et al.* 2018*a*), or algebraically grow (Yiantsios & Higgins 1989; Lister, Rallison & Rees 2010), eventually resulting in dripping droplets.

The problem of the dynamics of a thin film is usually studied within the context of the lubrication approximation. The model assumes much larger characteristic lengths in the directions which lay along the substrate than in the normal-to-the-substrate direction (Ruschak 1978; Wilson 1982; Babchin *et al.* 1983; Weinstein & Ruschak 2004).

In the case of an inclined substrate, the route from a flat film towards dripping drops still needs to be analysed. When the substrate is tilted with respect to the horizontal direction, the gravity component parallel to the substrate creates a flow. In this work, we consider a configuration with a permanent influx, in opposition to the case of cylindrical and spherical substrates in which a transient release of fluid is studied (Balestra *et al.* 2018*a*; Balestra, Nguyen & Gallaire 2018*b*). A strong modulation of the thickness along the direction perpendicular to the flow (spanwise direction) is identified as rivulet formation (Charogiannis *et al.* 2018). The presence of a predominant rivulet pattern when the inertia of the fluid is negligible was experimentally observed by Charogiannis *et al.* (2018). Similar rivulet patterns were observed by Rietz *et al.* (2017), in an experimental set-up where gravity was replaced by centrifugal acceleration. Lerisson *et al.* (2019) showed that a state characterized by lenses travelling on the rivulets may emerge, depending on the inclination angle and flow rate.

The stability analysis was performed by linearizing the flow equations around a constant thickness, revealing that the flat film solution is always unstable to perturbations (Brun *et al.* 2015). These authors found experimentally a link between dripping and the absolute instability of the flow, modelled with the one-dimensional lubrication equation. The model was refined introducing inertial and viscous extensional stresses (Scheid, Kofman & Rohlfis 2016; Kofman *et al.* 2018). These authors showed that the occurrence of the absolute instability does not predict the dripping satisfactorily.

In Lerisson *et al.* (2020) an experimental set-up able to continuously feed an inclined planar substrate with fluid was presented. Using a very viscous fluid such that inertial effects are negligible, the natural emergence of elongated, streamwise-oriented, steady patterns was observed. A detailed analysis of the appearance of these so-called rivulets was then performed, both when a spanwise-periodic forcing is imposed at the inlet and when the rivulets emerge naturally from the lateral boundaries of the experiment. The forced dynamics revealed that there is a narrow range of attainable spacings of rivulets. The nonlinear simulations agreed with the thickness measured in experiments, observing steady and streamwise-invariant rivulet states, periodic along the spanwise direction. The one-dimensional and saturated rivulet profile was recovered by simple static arguments, i.e. the equilibrium between capillary effects and hydrostatic pressure gradient

(Roman, Gay & Clanet 2020; Zaccaria *et al.* 2011; Duprat & Stone 2015). The correct shape was obtained imposing the local flow rate along the direction transverse to the rivulet profile.

In this work, we aim at rationalizing the observations of steady rivulet patterns by investigating the intrinsic rivulets selection and their stability.

The paper is organized as follows. We first introduce an experimental visualization for the evolution of the film when the inlet is steadily forced along the spanwise direction. A numerical study for an initial condition that mimics these experimental conditions, namely a regular pattern of sinusoidal perturbations in the spanwise direction, is performed. Periodic boundary conditions in all in-plane directions are imposed. The experimental and numerical results are then rationalized by a secondary stability analysis. We perturb the one-dimensional rivulet profile along the streamwise direction with a normal mode expansion and obtain a dispersion relation characterizing the secondary growth of lenses. We thus present a comparison of the secondary stability study with experimental measurements of the spatial amplification of disturbances over steady rivulets. The last section is devoted to the study of the emergence of rivulets from a flat film when the film is impulsively perturbed. We introduce a qualitative experimental visualization when the film is excited by a localized perturbation in the thickness, the results of which are numerically reproduced. A weakly nonlinear model is eventually proposed to rationalize these observations.

2. Experimental apparatus

The experimental apparatus is the same as that described in Lerisson *et al.* (2020) (see figure 1). The substrate is an orientable glass plate of length $\hat{L}_x = 600$ mm and width $\hat{W}_i = 300$ mm, whose angle with respect to the vertical is varied from $\theta = 20^\circ$ to $\theta = 80^\circ$. The fluid is silicon oil (Bluestar Silicons 47V1000) of density $\rho = 974$ kg m⁻³, viscosity $\mu = 1089$ mPa s and surface tension coefficient $\gamma = 21$ mN m⁻¹. The oil is injected through a horizontal rectangular opening of a reservoir and flows beneath the substrate. The flow rate is driven by the height difference with another reservoir that creates a hydrostatic pressure gradient. The flow rate can be varied by changing the height difference of the two reservoirs. The system is designed in such a way that it is possible to steadily modify the inlet condition in the spanwise direction by adding a sinusoidal or a comb-like blades (see sketches in figure 1a). The sinusoidal blade is placed below the inlet with an angle of 30° with respect to the substrate, and the fluid fills the gap between the glass and the blade. Systematic measurements of the thickness give a thickness perturbation amplitude of $\simeq 250$ μ m. The comb-like blade presents teeth of thickness $\hat{t}_i = 1$ mm, streamwise size of $\hat{l}_{dt} = 5$ mm and spanwise size of 2 mm. The teeth occlude the inlet and the fluid covers them by capillarity.

The volumic flow rate q is measured by weighing the oil leaving the substrate for 180 s. We define the equivalent Nusselt thickness h_N as well as the reduced capillary length l_c^* :

$$h_N = \left(\frac{3\nu q}{\hat{W}_i g \cos(\theta)} \right)^{1/3}, \quad l_c^* = \frac{l_c}{\sqrt{\sin(\theta)}}, \quad (2.1a,b)$$

where $l_c = \sqrt{\gamma/(\rho g)}$ is the capillary length, g the gravity acceleration and $\nu = \mu/\rho$ the kinematic viscosity. We define a coordinate system $(\hat{x}, \hat{y}, \hat{z})$, where \hat{x} , \hat{y} and \hat{z} are respectively the streamwise, spanwise and normal-to-the-substrate directions.

We employ a qualitative visualization technique based on shadowgraphs that are constructed looking at the distortion of the rays coming from a point light source

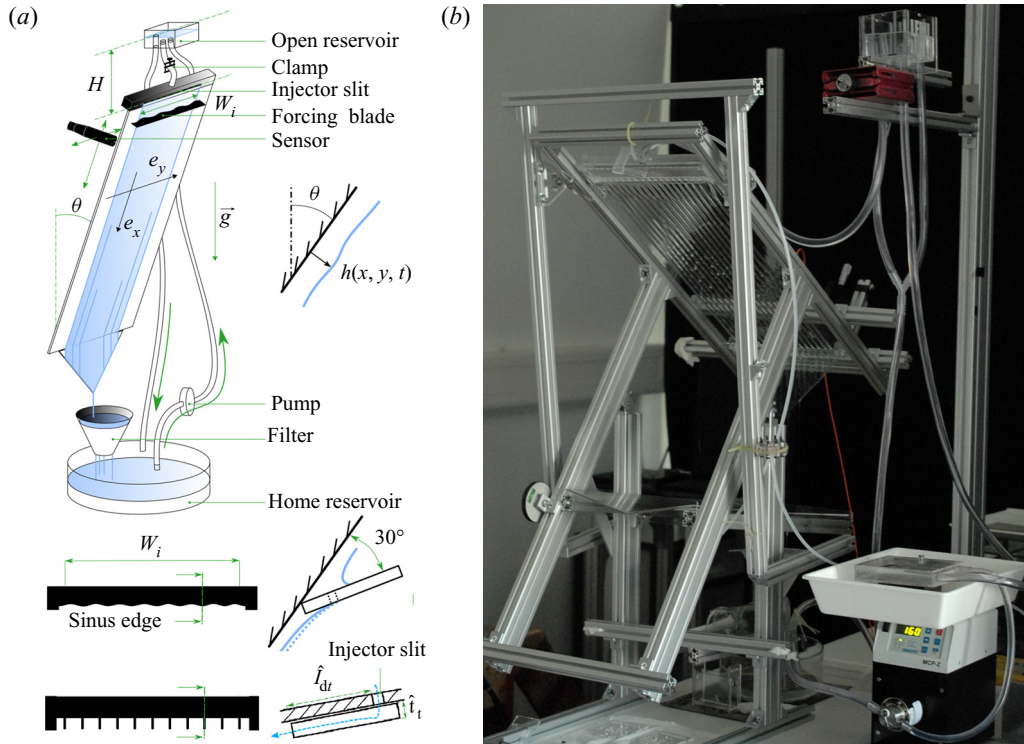


FIGURE 1. (a) Sketch of the experimental apparatus with the detail of the sinusoidal and comb-like blades for the steady forcing at the inlet along the spanwise direction. (b) Photo of the experimental apparatus.

through the liquid film. The surface deformation will focus or defocus the initially homogenous light and forms patterns that are highly sensitive to slight deformations. The combination of small and large deformations (Settles 2001; Moisy, Rabaud & Salsac 2009) within the same experiment makes the visualization impossible to relate to quantitative measurements of the thickness amplitude. However, the experiment gives access to the phases of perturbations, and thus to qualitative observations of the emerging pattern.

We measure the film thickness using the confocal chromatic sensor STIL-CCS located on the upper part of the glass plate. We choose an acquisition rate of 100 Hz. The position of the sensor can be adjusted in the normal-to-the-substrate and spanwise directions once the streamwise location is selected.

3. Observations of the secondary stability and instability of rivulets

3.1. Experimental observations

In this section, we briefly present selected results from the study of Lerisson *et al.* (2020) in the presence and absence of the spanwise inlet forcing devices shown in figure 1(a). Figure 2(a) shows a film thickness distribution obtained using an absorption technique (reproduced from Lerisson *et al.* 2020). The inlet spanwise thickness profile is amplified, and streamwise-saturated and steady rivulets are observed downstream. The saturated rivulets are periodic along the spanwise direction. There is a narrow range of attainable spacings, when the inlet is forced, around the value $\hat{L}_r = 2\pi\sqrt{2}l_c^*$ (value shown

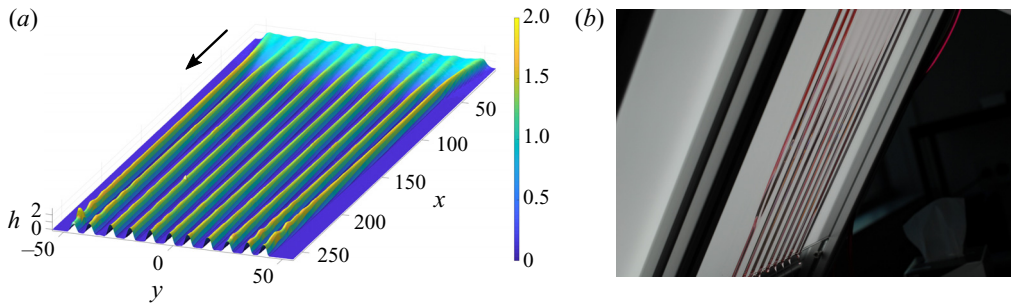


FIGURE 2. (a) Film thickness for $\theta = 39^\circ$ and $h_N = 1515 \mu\text{m}$ ($u = 1.5$), steady inlet forcing with the sinusoidal blade at the wavelength $\hat{L}_f = 2\pi\sqrt{2}l_c/\sqrt{\sin\theta}$, extracted from Lerisson *et al.* (2020). The thickness is measured with the absorption method and normalized by the flat film thickness h_N . The in-plane distances are normalized by the reduced capillary length $l_c/\sqrt{\sin\theta}$. (b) Typical rivulet pattern in the absence of the inlet forcing devices (figure 1a), $\theta = 20^\circ$.

in figure 2a), i.e. the most amplified wavelength in the dispersion relation of the flat film. Interestingly, even in the absence of the spanwise inlet forcing devices, the predominant spacing of the emerging rivulet structures is \hat{L}_r (see figure 2b).

However, far downstream in figure 2(a), oscillations appear on the rivulet profiles. These oscillations are amplified and rivulets carrying travelling lenses are observed, for these values of angle and flow rate.

3.2. Numerical observations

The aim of this section is to numerically study the emerging patterns for an initial condition that mimics the experimental conditions described in the previous section.

We consider a gravity-driven thin film of viscous Newtonian fluid flowing under a planar substrate inclined with respect to the vertical with an angle θ . We introduce the following non-dimensionalization:

$$x = \hat{x}/l_c^*; \quad y = \hat{y}/l_c^*; \quad z = \hat{z}/h_N; \quad t = \hat{t}/\tau^*, \quad (3.1a-d)$$

where $\tau^* = \nu l_c^2/h_N^3 \sin^2(\theta)g$ is the characteristic time scale of the Rayleigh–Taylor instability. The numerical model for the evolution of the film thickness h is the lubrication equation in which the complete expression of the curvature is retained (Ruschak 1978; Wilson 1982; Weinstein & Ruschak 2004):

$$\partial_t h + u h^2 \partial_x h + \frac{1}{3} \nabla \cdot [h^3 \nabla h + h^3 \nabla \kappa] = 0, \quad (3.2)$$

where ∇ operates in the (x, y) directions, $u = \cot(\theta)\tilde{l}_c^*$ and $\tilde{l}_c^* = l_c^*/h_N$. The linear advection velocity u corresponds to the surface film velocity at which linear interface thickness perturbations with respect to a flat condition are advected downstream (Brun *et al.* 2015). In physical quantities, an increase of the parameter u implies a decrease of the flow rate (since u is inversely proportional to h_N) or θ . The curvature κ reads

$$\kappa = \frac{\partial_{xx} h (1 + (\partial_y h)^2) + \partial_{yy} h (1 + (\partial_x h)^2) - 2 \partial_{xy} h \partial_x h \partial_y h}{(1 + (\partial_x h)^2 + (\partial_y h)^2)^{3/2}}. \quad (3.3)$$

The two-dimensional equation is implemented in COMSOL Multiphysics. We use the built-in finite elements method solver, exploiting cubic elements with Lagrangian

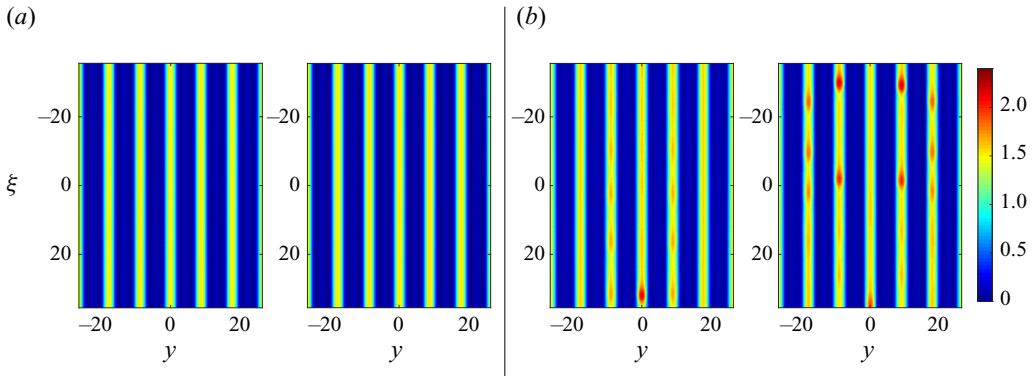


FIGURE 3. Nonlinear response in the case of a streamwise-invariant sinusoidal initial condition, for (a) $u = 5.45$ and (b) $u = 1.5$. From left to right: $t = 1000$, $t = 1200$. Results are reported in the moving reference frame at the linear advection velocity ($\xi = x - ut$, y).

shape functions and a fully implicit time solver. The largest mesh element size is half of the reduced capillary length \tilde{l}_c^* . The domain size is $L_x \times L_y$, where $L_x = 231$ and $L_y = 106$, leading to approximately 50 000 elements. A convergence analysis was performed, showing that convergence is achieved for this characteristic size of the elements. This characteristic element size was also validated by the experimental and numerical comparisons in Lerisson *et al.* (2020). The equations are solved for the variables (h, κ) . For all the considered cases, periodic boundary conditions are used.

Experimentally, in the absence of the spanwise inlet perturbation device described in figure 1(a), the rivulet spacing is the one dictated by the most amplified mode in the flat film dispersion relation, i.e. $L_r = 2\pi\sqrt{2}$ (Lerisson *et al.* 2020). We numerically study the nonlinear time evolution when a streamwise-invariant sinusoidal initial condition is considered. We choose as initial condition a sinus of wavelength $L_r = 2\pi\sqrt{2}$:

$$h(x, y, t = 0) = \bar{h}_N \left(1 + A \cos \left(\frac{2\pi y}{L_r} \right) \right), \tag{3.4}$$

where $A = 10^{-2}$, and $\bar{h}_N = 0.54$ is the initial value of the thickness that gives, for a pure streamwise saturated structure, the same local flow rate in the streamwise direction as a flat film of thickness $h = 1$ (§ 5.3 in Lerisson *et al.* 2020).

We introduce the moving reference frame at the linear advection velocity u ($\xi = x - ut$, y). Figure 3 shows the evolution of the thickness with time for (a) $u = 5.45$ and (b) $u = 1.5$. For visualization purposes, we focus in the region $\xi \in [-8\pi\sqrt{2}, 8\pi\sqrt{2}]$ and $y \in [-6\pi\sqrt{2}, 6\pi\sqrt{2}]$. In both cases, the streamwise invariant initial condition is amplified and reaches, at $t = 800$, a saturated state in the streamwise direction. For (a) $u = 5.45$, we do not observe any further evolution of the pattern for $t > 800$. For (b) $u = 1.5$, at $t = 800$ the rivulet profiles saturate. For $t > 800$, however, streamwise thickness perturbations grow, and at $t = 1200$ the flow is characterized by lenses travelling on the rivulets.

The streamwise-invariant sinusoidal initial condition is amplified leading to a rivulet pattern saturated in space and time, periodic along the spanwise direction. The absence (respectively presence) of observable streamwise perturbations on the rivulet profiles at high (respectively low) values of u suggests that the stability of the rivulet profile to streamwise perturbations may be directly related to the linear advection velocity.

The experimental observations of predominant spanwise-periodic rivulet patterns and the occurrence of lenses on the rivulets are confirmed by the nonlinear simulations with periodic boundary conditions. In the following, we aim at rationalizing the emergence of predominant rivulet structures and their destabilization.

4. Secondary stability analysis of rivulets

In § 3.1 it was experimentally shown that rivulet structures grow in the domain and saturate to a steady and spanwise-periodic state, invariant along the streamwise direction. However, for low values of u and at large distances from the inlet, the rivulet profile undergoes an instability and travelling lenses emerge on the rivulet structures, as shown in figure 2(a). The saturation of the rivulet structures and the occurrence of lenses was also observed in the nonlinear numerical simulation of figure 3. No lateral interactions between rivulets are observed as the lenses grow. Here, we study the robustness of the saturated rivulet pattern via a secondary stability analysis. We first introduce the steady, streamwise-invariant and spanwise-periodic rivulet profile $H_r(y)$, and then we focus on its local stability properties when perturbed along the streamwise direction, x . The validity of the local stability analysis is limited to the regions where steady and one-dimensional rivulets are observed.

4.1. Base flow

In this section, we define the saturated rivulet profile $H_r(y)$, serving as base flow for the local stability analysis. The numerical base flow is the large-time solution ($t = 10\,000$) of the one-dimensional model presented in § 5 of Lerisson *et al.* (2020). The profile, of periodic wavelength L_r , is given by a one-dimensional model in which the flow rate in the streamwise direction coincides with the one of a flat film of thickness $h = 1$, leading to a mean value $\bar{h}_N = 0.54$ of the thickness of the rivulet. The numerical procedure revealed that the rivulet profile is slowly saturating to a steady state $H_r(y)$. In figure 4, we report the numerical periodic profile at $t = 10\,000$ (solid line) used for the stability analysis. The rivulet is characterized by a central lobe of large thickness that saturates to a steady profile described by the pendulum equation (red circles in figure 4), while the side lobes (of very low thickness) are slowly draining with a power law $t^{-1/2}$ (Lister *et al.* 2010). It is remarkable that, with the considered non-dimensionalization, the profiles are independent of u , i.e. there is a unique rivulet shape (Lerisson *et al.* 2020). The numerical profile agrees well with the experimental results (dots in figure 4) and can therefore be safely used as base flow $H_r(y)$ for the stability analysis.

4.2. Dispersion relation

Following the classical approach of the local stability analysis, we consider as a base state the single, spanwise-periodic and steady rivulet $H_r(y)$ described in § 4.1. The quasi-steadiness of the rivulet profile allows us to neglect the slow evolution of the side lobes at long times and thus to consider a normal mode expansion in time and along the direction in which the base state is invariant, i.e. the streamwise direction x (Schmid, Henningson & Jankowski 2002). The spanwise periodicity governing the base state $H_r(y)$ is also enforced on the perturbation. The following normal mode decomposition is therefore used:

$$h(x, y, t) = H_r(y) + \varepsilon \tilde{\eta}(x, y, t) = H_r(y) + \varepsilon \eta(y) e^{i(k_x x - \omega t)}, \quad \varepsilon \ll 1, \quad (4.1)$$

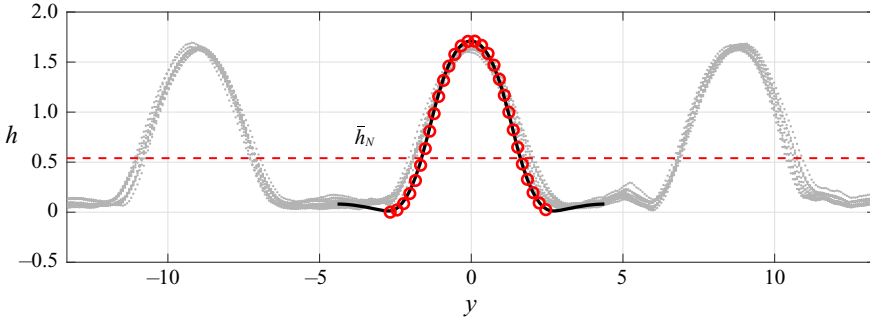


FIGURE 4. Periodic rivulet profile (black line) used for the stability analysis, compared with the results of the pendulum equation of § 5.4 of Lerisson *et al.* (2020) (red circles), and with the experimental results for three central rivulets (grey dots), from Lerisson *et al.* (2020), for 10 transverse measurements at two different streamwise locations, at $\theta = 39^\circ$ and different h_N . The red dashed line denotes the mean thickness \bar{h}_N of the rivulet.

where $\tilde{\eta}$ is the thickness perturbation with respect to the base flow profile $H_r(y)$. By considering the two-dimensional nonlinear equation (3.2) and introducing the normal mode decomposition (4.1), one obtains, up to $O(\varepsilon)$

$$\begin{aligned} \varepsilon \partial_t \tilde{\eta} + \varepsilon u H_r^2 \partial_x \tilde{\eta} + \frac{1}{3} \partial_y \left[H_r^3 \left(\frac{dH_r}{dy} + \frac{d\kappa_{(0)}}{dy} \right) + \varepsilon H_r^3 \partial_y \tilde{\eta} \right. \\ \left. + \varepsilon H_r^3 \partial_y \tilde{\kappa}_{(1)} + 3\varepsilon H_r^2 \left(\frac{d\kappa_{(0)}}{dy} + \frac{dH_r}{dy} \right) \tilde{\eta} \right] + \frac{\varepsilon}{3} \partial_x [H_r^3 (\partial_x \tilde{\kappa}_{(1)} + \partial_x \tilde{\eta})] = 0, \end{aligned} \quad (4.2)$$

where $\kappa_{(0)}$ is the base flow curvature, i.e. (3.3) evaluated for the base flow $H_r(y)$, $\kappa_{(0)} = (d^2 H_r / dy^2) / (1 + (dH_r / dy)^2)^{3/2}$. Furthermore, $\tilde{\kappa}_{(1)}$ is the first-order term of the curvature, i.e. the Jacobian of the curvature evaluated in the base flow and applied to $\tilde{\eta}$ ($\tilde{\kappa}_{(1)} = [\partial_{\tilde{\eta}} \kappa(H_r)] \tilde{\eta}$). The full expression of the operator $\partial_{\tilde{\eta}} \kappa(H_r)$ is reported in appendix A. Deriving this expression with respect to x and y , we obtain $\partial_x \tilde{\kappa}_{(1)} = ik_x \kappa_{(1)}(y) \exp(i(k_x x - \omega t))$ and $\partial_y \tilde{\kappa}_{(1)} = (d\kappa_{(1)} / dy)(y) \exp(i(k_x x - \omega t))$.

At $O(1)$ the base flow equation is recovered, while at $O(\varepsilon)$ one obtains the following evolution equation for the perturbation:

$$\begin{aligned} -i\omega \eta + ik_x u H_r^2 \eta + \frac{1}{3} \frac{d}{dy} \left[3H_r^2 \left(\frac{dH_r}{dy} + \frac{d\kappa_{(0)}}{dy} \right) \eta \right. \\ \left. + H_r^3 \left(\frac{d\kappa_{(1)}}{dy} + \frac{d\eta}{dy} \right) \right] - \frac{1}{3} k_x^2 [H_r^3 (\kappa_{(1)} + \eta)] = 0, \end{aligned} \quad (4.3)$$

which is the dispersion relation $D_r(\omega, k_x) = 0$. The base flow $H_r(y)$ can be perturbed by (i) imposing the streamwise wavenumber $k_x \in \mathbb{R}$ and looking at the temporal evolution through the complex frequency $\omega \in \mathbb{C}$ (temporal stability analysis) or (ii) imposing a temporal forcing of real frequency ω and looking at the spatial amplification of the perturbation, embodied by the complex spatial wavenumber $k_x \in \mathbb{C}$ (spatial stability analysis).

The numerical implementation of (4.3) is performed in MATLAB by a spectral collocation Fourier method. Once discretized, the eigenfunction problem (4.3) becomes an eigenvalue problem. The temporal and spatial stability analyses are respectively solved

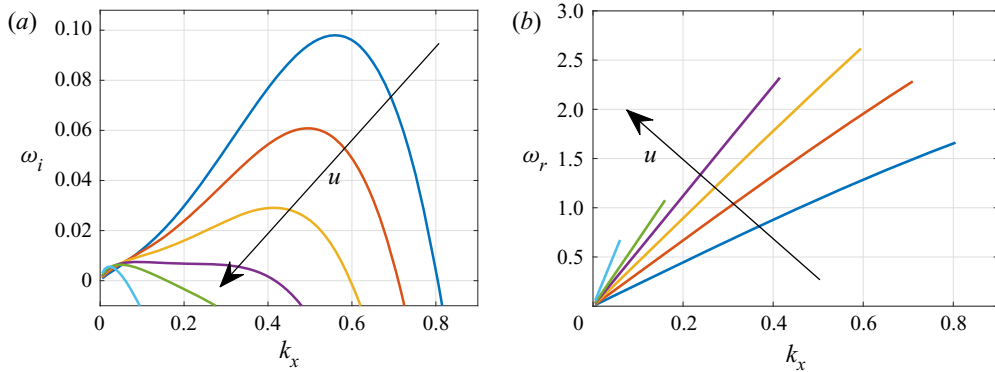


FIGURE 5. (a) Temporal growth rate ω_i and (b) real frequency ω_r as functions of the streamwise wavenumber k_x , from the temporal stability analysis, for $u = 1$ (blue line), $u = 1.5$ (red line), $u = 2$ (yellow line), $u = 2.5$ (purple line), $u = 3$ (green line), $u = 5$ (light blue line).

using the built-in MATLAB functions *eig* and *polyeig*. Numerical convergence is achieved for 100 collocations points. A preparatory analysis on the numerical rivulet profile $H_r(y)$ used as base flow for the stability analysis revealed a variation of the eigenvalues of the order of the numerical discretization, as long as $t > 5000$.

4.3. Temporal stability analysis

In this section, we report the results for the temporal stability analysis. Positive (respectively negatives) values of the temporal growth rate $\text{Im}(\omega) = \omega_i$ denote unstable (respectively stable) wavenumbers. A preliminary analysis on the spectrum revealed that all the eigenvalues have negative ω_i for all k_x , except one that is analysed in the following.

In figure 5(a) we report the variation of ω_i with k_x , for different values of u . The dispersion relations are characterized by a local maximum associated with the dominant wavenumber, and by a value of the wavenumber beyond which the temporal growth rate is negative (the cutoff wavenumber), i.e. perturbations with wavenumber larger than the cutoff are damped. Rivulets are strongly stabilized as the value of u increases. For $u = 1$ the growth rate ω_i presents its maximum value at a dominant wavenumber close to $k_x = 0.56$, while the cutoff wavenumber $k_x^{cut} = 0.8$. An increase of u quickly quenches large wavenumbers. Both the dominant growth rate and the cutoff wavenumber decrease. At $u = 5$, $k_x^{cut} \sim 10^{-2}$, with $\max(\omega_i) \sim 10^{-3}$. For these values of u , the unstable wavelengths are of the order of one hundred reduced capillary lengths. The real frequency $\text{Re}(\omega) = \omega_r$ increases slightly less than linearly with k_x (figure 5b). The resulting phase velocities ω_r/k_x increase as u increases.

In figure 6(a) we show the real (dashed-dotted line) and imaginary (dashed line) parts of the mode $\eta(y)$ for the dominant wavenumber $k_x = 0.5$, normalized by the maximum modulus $\max(|\eta|)$, for $u = 1.5$. The mode is non-zero only in the steady central lobe region. For the same value of u , in figure 6(b) we report a three-dimensional plot of the linear combination of the base flow $H_r(y)$ (extended in the x direction along which it is invariant) with the mode at the dominant wavenumber (normalized by the maximum modulus), i.e. $h(x, y) = H_r(y) + A \text{Re}(\eta(y) \exp(ik_x x))$, with $A = 0.25$ an arbitrary amplitude for visualization purposes. The resulting pattern is characterized by rivulets that carry lenses. The temporal dependence of the mode, which is not represented

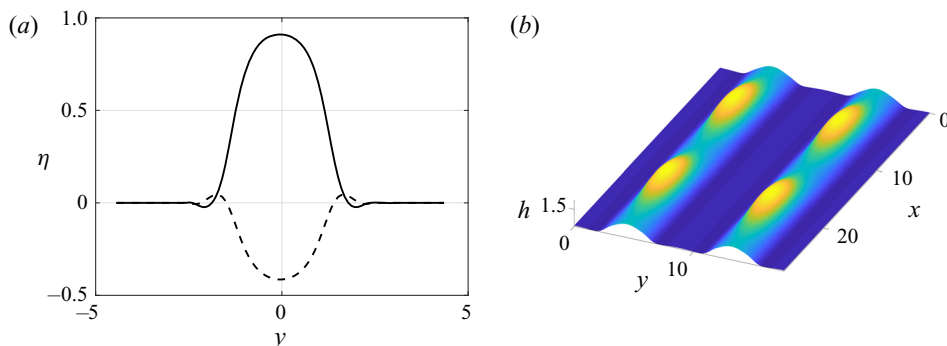


FIGURE 6. Temporal stability analysis, $u = 1.5$. (a) Real (solid line) and imaginary (dashed line) parts of the eigenvector $\eta(y)$, for the dominant wavenumber $k_x = 0.5$, normalized by the maximum modulus. (b) Linear combination of the base flow $H_r(y)$ (extended in the x direction along which it is invariant) with the mode at the dominant wavenumber (normalized with the maximum modulus), i.e. $h(x, y) = H_r(y) + A \operatorname{Re}(\eta(y) \exp(ik_x x))$. $A = 0.25$ is an arbitrary amplitude for visualization purposes.

in figure 6(b), is characterized by a growing amplitude $\exp(\omega_r t)$ and by an oscillating behaviour $\exp(i\omega_i t)$. The presence of a non-zero real part of ω (figure 5b) implies that the perturbations are oscillating in time at fixed locations. This effect is related to the advection as lenses are travelling along the streamwise direction.

The stability analysis reveals the occurrence of a secondary instability of the saturated and one-dimensional rivulets, which is located in the steady central lobe and leads to a pattern characterized by lenses that travel on the rivulets. Nevertheless, an increase in the advection u induces a very strong stabilization and only very large wavelengths remain slightly unstable. The stabilization is related to the advection term. In particular, perturbations in regions of different thickness experience different advection velocities, proportional to uH_r^2 (Kalliadasis *et al.* 2012). Regions of higher thickness travel faster than regions of lower thickness, leading to a steepening of the interface profile and eventually to a capillary levelling of perturbations. This steepening–levelling mechanism is all the more pronounced as u is large. Small wavelengths, which present high interface gradients, are progressively stabilized with u , leading to a cutoff wavelength of the order of $10^2 l_c^*$ at $u = 5$. In the numerical simulation of figure 3(a) the resulting pattern does not show any appreciable streamwise perturbations since the cutoff wavelength ($L_c = 2\pi/k_x^{cut} \approx 2 \times 10^2$) is of the order of the maximum acceptable wavelength fitting in the domain. These results are consistent with the experimental observations of Lerisson *et al.* (2020) when large values of u are considered. For $u > 3$, only very large wavelengths are unstable and they are eventually suppressed because of the size of the experiment ($2 \times 10^2 l_c^* < L_x < 3 \times 10^2 l_c^*$).

4.4. Spatial stability analysis

In this section, we study the spatial stability properties of the rivulet base flow $H_r(y)$ introduced in § 4.1. The saturated rivulet profile is perturbed with a temporal harmonic perturbation of real frequency $\omega = \omega_r$ and we look for the spatial evolution of the perturbation, in terms of spatial growth rate $-\operatorname{Im}(k_x)$ and streamwise wavenumber $\operatorname{Re}(k_x)$ through the dispersion relation $D_r(k_x, \omega)$ ((4.3)). Positive values of the spatial growth rate denote unstable configurations associated with downstream propagating waves (Huerre &

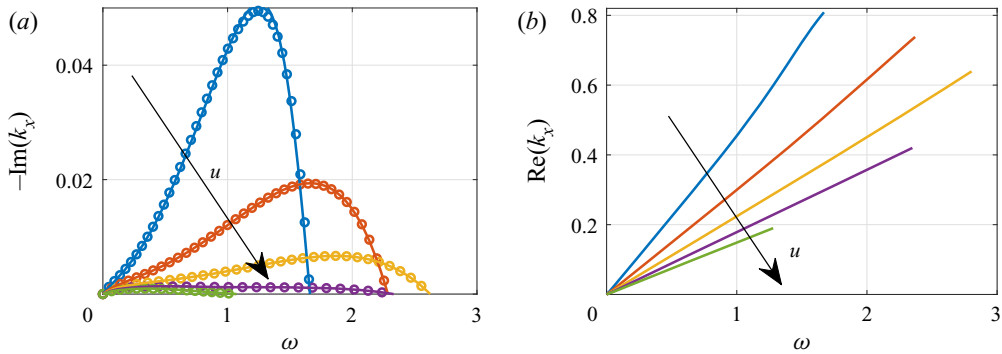


FIGURE 7. (a) Spatial growth rate and (b) streamwise wavenumber as functions of ω , from the spatial stability analysis, for $u = 1$ (blue line), $u = 1.5$ (orange line), $u = 2$ (yellow line), $u = 2.5$ (purple line), $u = 3$ (green line). The circles identify the values of the spatial growth rate obtained by the Gaster transformation.

Rossi 1998; Schmid *et al.* 2002; Gallaire & Brun 2017). The spectrum is characterized by only one unstable mode associated with downstream propagating waves, which is described in the following.

In figure 7(a) we report the spatial growth rate $-\text{Im}(k_x)$ as a function of ω . The spatial growth rate presents a behaviour similar to the temporal growth rate of § 4.3, i.e. characterized by a maximum (dominant) value and a cutoff frequency beyond which perturbations are damped. The dominant value of $-\text{Im}(k_x)$ strongly decreases with u , while its associated dominant frequency presents a non-monotonic behaviour. The same non-monotonic behaviour is observed in the cutoff frequency. The streamwise wavenumber $\text{Re}(k_x)$ (figure 7b) shows, to a good approximation, a linear dependence with ω . For fixed ω , the value of $\text{Re}(k_x)$ decreases with u .

The results of the spatial stability analysis are compared with those of the temporal stability analysis, suitably rescaled by the Gaster transformation (Gaster 1962), valid for strongly convectively unstable systems (see appendix B for details). Within this approximation, from the temporal stability analysis of § 4.3 (labelled with (T)) we retrieve the spatial stability analysis properties (labelled with (S)) through the relations

$$\omega_r(S) = \omega_r(T), \quad \text{Re}(k_x(S)) = \text{Re}(k_x(T)), \quad \text{Im}(k_x(S)) = -\frac{\omega_i(T)}{\frac{\partial \omega_r}{\partial k_x}(T)}. \quad (4.4a-c)$$

The results of the Gaster transformation (4.4a-c) (circles) are in good agreement with the spatial stability analysis results in figure 7(a), for $u > 1$. In appendix B we report the results for $u < 1$, where the Gaster transformation prediction deviates from the spatial stability analysis results.

In the following, we experimentally investigate the link between the spatial stability analysis and the observable dynamics.

5. Experimental measurements of the rivulet secondary instability

5.1. Methods

As described in § 3.1, steady rivulets invade the experiment and saturate along the streamwise direction (figure 2). At a certain distance from the inlet, streamwise oscillations

on the rivulet profiles grow and evolve into travelling lenses. We investigate the dependence of the overall dynamics and the amplitude of lenses with the parameters, by exploring different angles $40^\circ < \theta < 80^\circ$ and thicknesses in the range $0.12 < h_N/l_c < 1$ (related to the flow rate by (2.1a,b)). Note that $u = \cot(\theta)l_c/\sqrt{\sin\theta}h_N$, i.e. high values of the linear advection velocity correspond to low values of the flow rate or θ . We modify the inlet condition using the spanwise comb-like blade (figure 1a) with the optimal spacing predicted by the flat film linear dispersion relation, i.e. $\hat{L}_r = 2\pi\sqrt{2}l_c^*$. The requirement of a reasonably small and constant error in a large range of the flow parameters, exempted from a case-dependent calibration procedure, makes the confocal chromatic sensor STIL-CCS a suitable candidate. The latter is placed at the end of the plate to measure the variation of the amplitude of lenses oscillations as a function of θ and h_N/l_c .

The procedure is the following. We place the comb in position, and we wait the time necessary for rivulets to invade the whole domain. We then measure the central rivulet maximum thickness $\hat{h}_{max}(t)$ for 20 periods. This leads to a registration time T that goes from 20 to 2000 s, depending on the angle. Once the data are registered, the flow rate is increased. We wait the time necessary to advect all the transient effects away from the glass plate; this varies from one minute, for $\theta = 40^\circ$, to one hour, for $\theta = 80^\circ$. Assuming the saturated rivulet profile (figure 4), we transform the point measurement of the maximum thickness in an estimate of the integral flux (i.e. h_N in (2.1a,b)) by introducing the average thickness \hat{h} as follows:

$$\hat{h} = \left(\frac{3}{T} \int_0^T \frac{\hat{h}_{max}^3(t)}{3} dt \right)^{1/3}, \quad h_N = \hat{h}/1.71, \tag{5.1a,b}$$

being $\hat{h}_{max} = 1.71h_N$ for a steady and saturated one-dimensional rivulet (Lerisson *et al.* 2020). The deviation $\hat{\Delta}$ from the average thickness value is computed as

$$\hat{\Delta} = \sqrt{\frac{1}{T} \int_0^T (\hat{h}_{max}(t) - \hat{h})^2 dt}, \tag{5.2}$$

which is non-dimensionalized using the capillary length, i.e. $\Delta = \hat{\Delta}/l_c$. Two typical measurements are reported in figure 8.

5.2. Results

In figure 9 we report the deviation Δ as a function of h_N/l_c , for different angles θ . At low values of h_N/l_c , Δ is constant at a plateau value around $\Delta \sim 10^{-3}$. The plateau corresponds to the resolution of the optical sensor and is of order 1 μm . At higher values of h_N/l_c , Δ increases with h_N/l_c . We measure an increase of Δ of two decades.

The amplitude of the oscillations at the end of the plate is compared with the theoretical findings of the spatial stability analysis. The spatial amplification at a distance x of a temporal perturbation Δ_0 on a fully developed rivulet profile reads

$$\Delta/\Delta_0 = \exp(-\text{Im}(k_x)x). \tag{5.3}$$

We assume that the observable disturbances are the inlet ones as they are amplified on the largest distance, i.e. $x = L$. The perturbation amplitude Δ_0 originates from background noise that is below the sensitivity of our measurement sensor ($\sim 1 \mu\text{m}$). We assume that

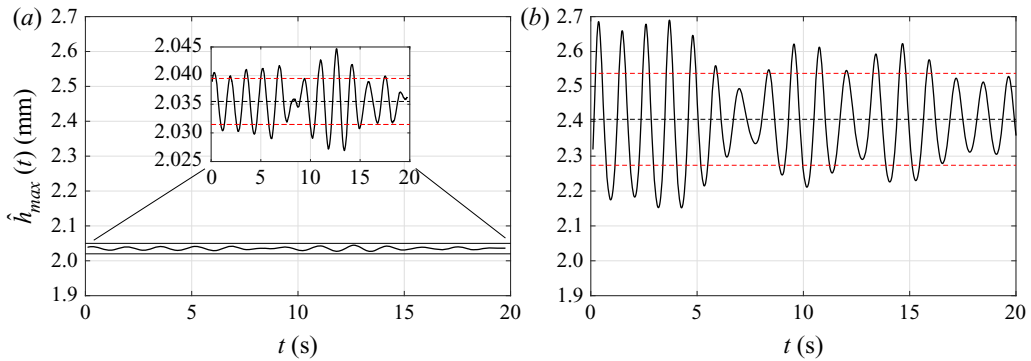


FIGURE 8. Registered maximum height $\hat{h}_{max}(t)$ of the rivulet, for (a) $\theta = 40^\circ$ and $h_N = 1190 \mu\text{m}$, (b) $\theta = 40^\circ$ and $h_N = 1418 \mu\text{m}$. The black dashed line denotes \hat{h} , and the red dashed lines $\hat{h} \pm \hat{\Delta}$. (a) $u = 1.85$, $\hat{\Delta} = 0.004$ and (b) $u = 1.57$, $\hat{\Delta} = 0.132$.

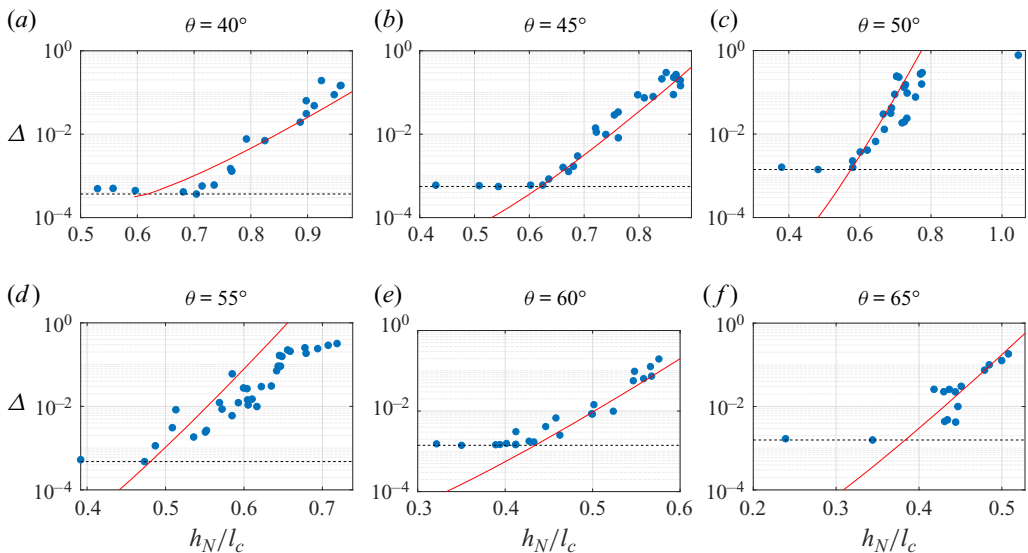


FIGURE 9. Values of Δ (blue dots) as a function of h_N/l_c , for different values of θ . The black horizontal line denotes the plateau value due to the resolution of the optical sensor. The red lines denote the amplification estimated using the spatial stability analysis of § 4.4 and the size of the plate, i.e. $\Delta = \Delta_0 \exp(-\text{Im}(k_x)L)$, with an initial amplitude chosen to obtain a good fit of the experimental data, (a) $\Delta_0 = 2 \times 10^{-4}$, (b) $\Delta_0 = 3 \times 10^{-5}$, (c) $\Delta_0 = 7.5 \times 10^{-6}$, (d) $\Delta_0 = 1 \times 10^{-6}$, (e) $\Delta_0 = 1.5 \times 10^{-5}$, (f) $\Delta_0 = 3 \times 10^{-6}$.

the noise triggers the dominant mode described in §§ 4.3 and 4.4, and that Δ_0 is constant for a fixed angle. Note that the dominant spatial growth rate changes with h_N/l_c since the value of u is varied.

In figure 9 the red lines denote the theoretical values of Δ for an inlet perturbation amplitude Δ_0 chosen to obtain a good fit of the experimental data. The measurement is then not a direct measure of the spatial growth rate, but of the variation of the spatial growth rate with the parameters. The variation of the deviation with the parameters well agrees with the linear prediction.

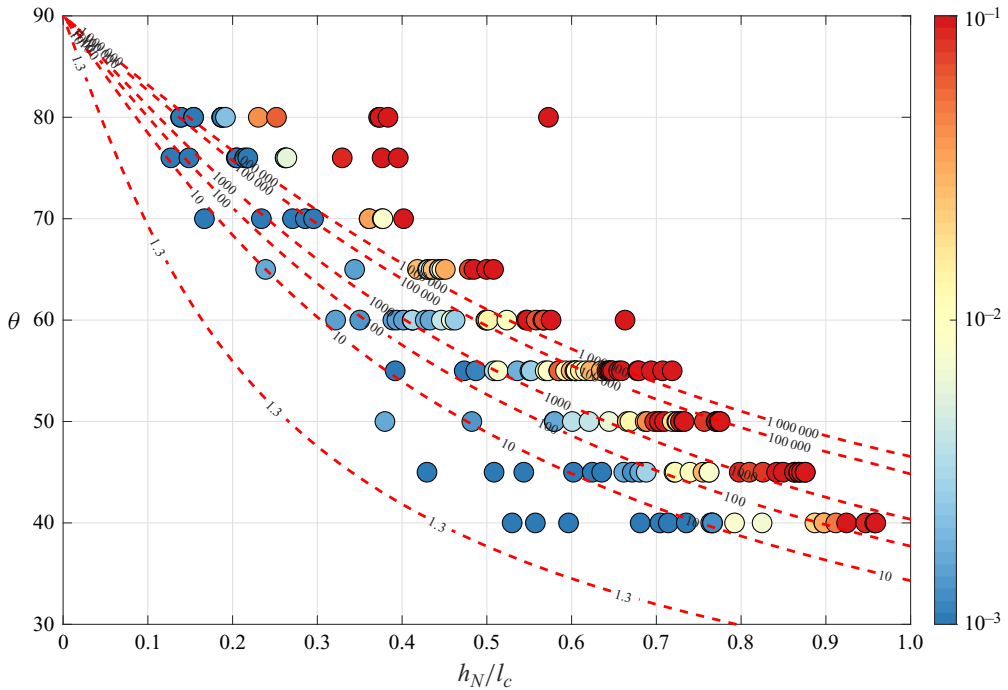


FIGURE 10. Results of the analysis in the $(\theta, h_N/l_c)$ plane: experimental measurements of Δ (coloured dots) and inlet disturbance amplification $\Delta/\Delta_0 = \exp(-\text{Im}(k_x)L)$ evaluated by the spatial stability analysis of § 4.4 (red iso-contours).

In figure 10 the experimental measurements of Δ (coloured dots) are summarized and reported together with the spatial amplification Δ/Δ_0 obtained by the spatial stability analysis (red dashed lines). At low values of h_N/l_c the experimental values of Δ are below the resolution of the optical sensor. As h_N/l_c increases, Δ emerges from the measurement resolution and we observe an increase of two orders of magnitudes in the considered range of parameters. This strong increase can be correlated to the theoretical amplification curves. At very low values of h_N/l_c and inclination angles the theoretical amplification is of order $\Delta/\Delta_0 \sim 10^0$. Low values of the flow rate (h_N/l_c) or θ imply high values of u . In particular, the iso-level with value $\exp(-\text{Im}(k_x)L) = 1.3$ roughly corresponds to the case $u = 3.5$. As h_N/l_c and θ are increased the theoretical amplification rapidly grows.

Our analysis suggests that the occurrence of streamwise oscillations on the rivulet profile is strongly related to the advection. The measured deviations strongly vary with u . When high values of u are considered, the occurrence of a steady and saturated rivulet pattern is observed (figure 11a). For low enough values of u , a state characterized by lenses which travel on rivulets is observed (figure 11b), as shown in (Lerisson *et al.* 2019). Small variations in the advection lead to dramatic effects on the overall pattern dynamics. A change in the inclination of the plate of 10° , e.g. from $\theta = 60^\circ$ to $\theta = 50^\circ$ at $h_N/l_c = 0.55$, is enough to pass from a state characterized by large amplitude lenses to a rivulet pattern.

In the route to dripping, the formation of lenses can be interpreted as a secondary instability of steady and streamwise-saturated rivulets, in which the role of the advection is essential.

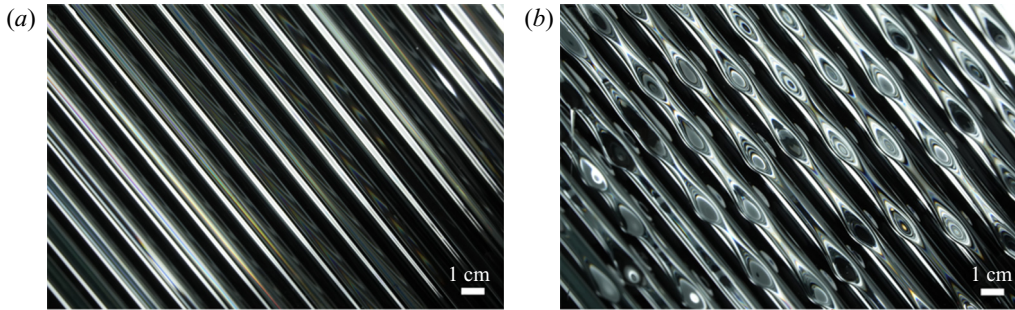


FIGURE 11. Representative patterns at $\theta = 45^\circ$ for (a) $h_N = 623 \mu\text{m}$, i.e. $h_N/l_c = 0.42$ and $u = 2.83$, characterized by rivulets, and for (b) $h_N = 1352 \mu\text{m}$, i.e. $h_N/l_c = 0.92$ and $u = 1.29$, characterized by rivulets which carry lenses.

6. Linear and nonlinear impulse response: breaking of isotropy and emergence of rivulets

In the previous sections, we numerically and experimentally studied the stability of steady and streamwise-saturated rivulet structures with respect to streamwise perturbations, and the link with the growth of travelling lenses. As observed in [figure 2](#), the instability of rivulets and the consequent emergence of lenses is preceded by the formation of rivulet structures that invade the whole domain. Hereafter, we aim at giving a physical insight into the predominance of rivulet structures by studying the response of the flat film to an impulsive perturbation localized in space and time, i.e. the impulse response.

6.1. Experimental observation

In this section, we introduce a qualitative visualization of the evolution of a localized perturbation in the film thickness. The experimental apparatus is set without any inlet perturbation devices shown in [figure 1\(a\)](#). When high inclination angles and low flow rates are considered (i.e. high values of u), we experimentally observe a large region characterized by a uniform flat film where thickness perturbations from the lateral boundaries of the experiment do not penetrate ([Lerisson *et al.* 2020](#)). In this region, we trigger the destabilization with a thickness perturbation by blowing a puff of air with a syringe. The whole field is then projected on a screen via the shadowgraph technique and captured with a camera.

In [figure 12](#) we show the evolution of the perturbation with time. The initially localized perturbation is advected away in the streamwise direction with a constant velocity and spreads in the domain. The perturbation phase lines are concentric circles in the upstream part of the response. Nevertheless, the isotropy disappears in the downstream part. The shadowgraph reveals that the phase lines tend to be parallel to the streamwise direction, the effect becoming more and more evident as the time increases.

The presence of phase lines aligned with the streamwise directions suggests the existence of a wavefront characterized by streamwise structures, i.e. rivulets, when the flat film is perturbed using an impulse thickness perturbation. The selection of a streamwise wavefront is not related to the boundaries of the thin film in the experiment, i.e. the rivulets selection is intrinsic.

6.2. Numerical observation

Inspired by this experimental observation, in this section we numerically simulate the impulse response, via (3.2), for the same values of angle and flow rate used in the

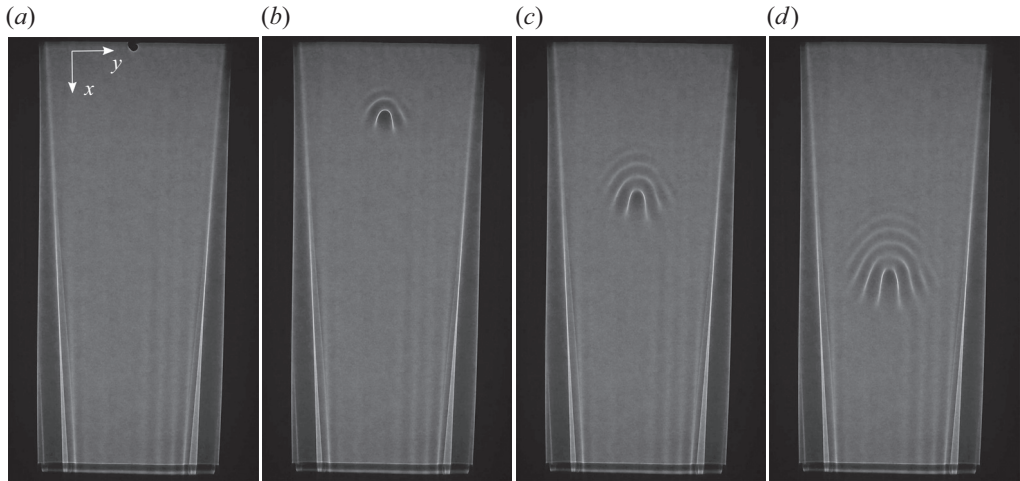


FIGURE 12. Shadowgraph visualization of an experimental impulse response, for $\theta = 20^\circ$ and $h_N = 1292 \mu\text{m}$, i.e. $u = 5.45$. Time increases going to the right and each snapshot is separated by 15 s. (a) $t = 0$ s, (b) $t = 15$ s, (c) $t = 30$ s and (d) $t = 45$ s.

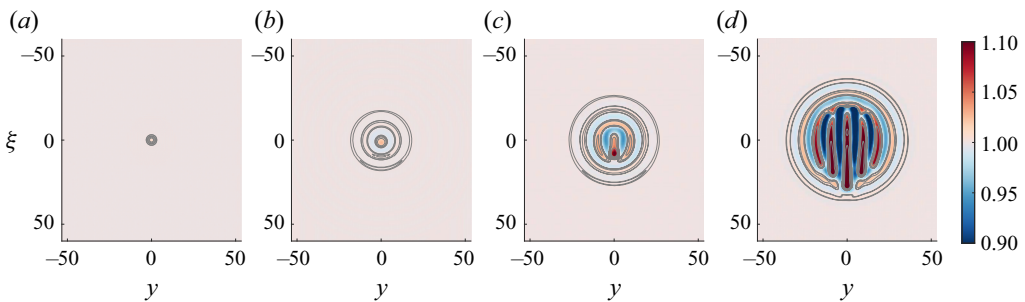


FIGURE 13. Impulse response, $\theta = 20^\circ$ and $h_N = 1292 \mu\text{m}$ ($u = 5.45$). The time increases from left to right and the time step is 30. Results are reported in the moving reference frame at the linear advection velocity ($\xi = x - ut, y$). (a) $t = 0$, (b) $t = 30$, (c) $t = 60$, (d) $t = 90$.

shadowgraph of [figure 12](#), i.e. $u = 5.45$, in a double-periodic domain. The initial condition is taken in the form

$$h(x, y, 0) = 1 + A \exp\left(-\frac{x^2 + y^2}{2}\right), \tag{6.1}$$

where $A = 10^{-2}$. In [figure 13](#) we plot the time evolution of the response in the moving reference frame ($\xi = x - ut, y$), from $t = 0$ to $t = 90$. In the moving reference frame, the response progressively invades the domain from the initial impulse location. At $t = 30$, we observe circular phase lines. At $t = 60$ the response loses its isotropy in the downstream part. At $t = 90$ streamwise structures are dominant in the downstream front of the response and they are also observable upstream.

In the moving reference frame, the response spreads from the initial impulse location, meaning that in the fixed reference frame, the response is advected downstream at the linear advection velocity u . The numerical evolution qualitatively agrees with the experimental observation of [§ 6.1](#). We first observe the evolution of the impulse response into an isotropic pattern. At large times, the response mostly evolve towards streamwise

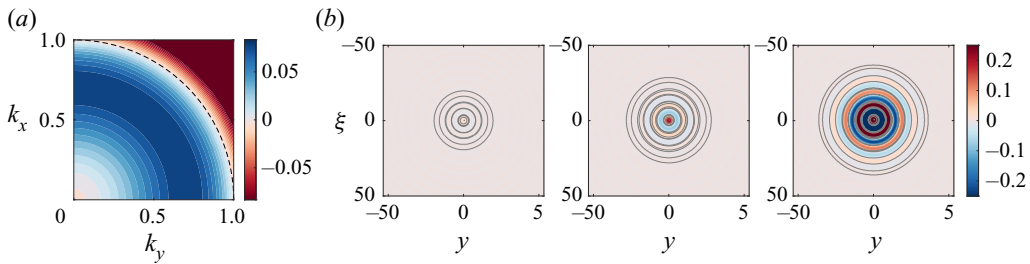


FIGURE 14. (a) Temporal growth rate ω_i as a function of k_x and k_y . (b) Linear impulse response, $u = 5.45$. The vertical and horizontal axes are respectively the streamwise and spanwise directions. From left to right: $t = 30$, $t = 60$, $t = 90$. Results are reported in the moving reference frame at the linear advection velocity ($\xi = x - ut$, y).

structures. However, the complicated form of (3.2), including nonlinear advection, hydrostatic pressure distribution and capillary effects, does not allow one to identify the physical mechanisms that lead to the emergence of streamwise structures observed in figures 12 and 13. Lerisson *et al.* (2020) furthermore observed that the rivulet propagation and growth are well described by the linear stability analysis of the flat film even at large amplitudes of the thickness perturbation, beyond the expected validity of the linear theory. Hereafter, we study the origin of the selection of rivulet structures by the linear and weakly nonlinear dynamics.

6.3. Linear response

Upon introduction of the decomposition $h = 1 + \varepsilon\eta$ ($\varepsilon \ll 1$) in (3.2), the linearized equation at $O(\varepsilon)$ for the evolution of the thickness perturbation η with respect to the flat film reads

$$\partial_t \eta + u \partial_x \eta + \frac{1}{3} [\nabla^2 \eta + \nabla^4 \eta] = 0. \quad (6.2)$$

The dispersion relation is recovered by introducing the normal mode decomposition $\eta \propto \exp[i(\mathbf{k} \cdot \mathbf{x} - \omega t)]$, with $\mathbf{k} = (k_x, k_y)$, where k_x and k_y denote respectively the streamwise and spanwise wavenumbers

$$\omega = uk_x + \frac{i}{3}(k^2 - k^4), \quad (6.3)$$

where $k = \sqrt{k_x^2 + k_y^2}$. The dispersion relation $D(\omega, k_x, k_y) = 0$ is characterized by an isotropic temporal growth rate ω_i , as shown in figure 14(a). The temporal frequency ω_r is linear in k_x and does not depend on k_y .

The initial condition for the numerical simulation is the thickness perturbation $\eta(x, y, 0) = A \exp(-x^2/2 - y^2/2)$, where $A = 10^{-2}$. The linear numerical simulation results for $u = 5.45$, in the moving reference frame ($\xi = x - ut$, y), are presented in figure 14(b). As time increases, the perturbation spreads in concentric circles from the initial impulse location. Similarly to the nonlinear simulation of figure 13, the response is advected away at the linear advection velocity u , in the fixed reference frame. The results can be rationalized considering the dispersion relation of (6.2). The wavepacket is non-dispersive since ω_r is linear in k_x . This means that there is no distortion of the wavepacket. Since the growth is isotropic, concentric circles invade the domain and at the

same time are advected downstream with constant velocity $\omega_r/k_x = u$. Higher values of u imply faster advection velocities. In the moving reference frame (ξ, y) , the (6.2) reads

$$\partial_t \eta + \frac{1}{3}[\nabla_{\xi y}^2 \eta + \nabla_{\xi y}^4 \eta] = 0, \quad (6.4)$$

where $\nabla_{\xi y}$ operates in the reference frame (ξ, y) . In this reference frame, the response spreads in perfectly isotropic concentric circles without being advected away. The linear dynamics agrees well with the early-time evolution of the nonlinear simulation shown in figure 13, when the amplitude of the perturbations is still very small. However, since the linearized dynamics is not able to capture the anisotropy of the pattern observed in the nonlinear simulation, we propose next a weakly nonlinear study.

6.4. Weakly nonlinear response: the Nepomnyashchy equation

We consider a weakly nonlinear model for the flow of a thin film on the underside of an inclined planar substrate. Following Kalliadasis *et al.* (2012), the derivation is based on a multiple scale approach combined with an asymptotic expansion. Under the assumption of small interfacial disturbances and $u = O(1)$, the weakly nonlinear dynamics for a thickness perturbation η with respect to the flat film reads

$$\partial_t \eta + 2u\eta \partial_\xi \eta + \frac{1}{3}[\nabla_{\xi y}^2 \eta + \nabla_{\xi y}^4 \eta] = 0, \quad (6.5)$$

where $\nabla_{\xi y}$ operates in moving the reference frame (ξ, y) . The equation is formally analogous to the Nepomnyashchy equation (Kalliadasis *et al.* 2012). We consider the evolution of the thickness perturbation η starting from a Gaussian impulse $\eta(\xi, y, 0) = A \exp(-\xi^2/2 - y^2/2)$ ($A = 10^{-2}$), in analogy with the linear simulation.

In figure 15(a) we report the thickness perturbation evolution. The initial localized perturbation spreads in the domain and is always centred in the vicinity of the initial impulse position, because of the moving reference frame. At $t = 30$ the perturbation has spread isotropically in the domain. Nevertheless, at $t = 60$, streamwise structures arise. At $t = 90$, the streamwise structures have invaded most of the perturbation region.

In figure 15(b) we show the two-dimensional Fourier energy spectrum of η , normalized by its maximum value. Since we are considering a real signal, the Fourier spectrum is symmetric with respect to the k_x and k_y axes. We thus report only the values in the first quadrant ($k_x > 0, k_y > 0$). At $t = 0$, we observe the Fourier spectrum of a Gaussian impulse, which is a Gaussian centred around $(k_x = 0, k_y = 0)$, i.e. the initial spectrum is isotropic. At $t = 30$ the energy is located in a region around $\sqrt{k_x^2 + k_y^2} = 1/\sqrt{2}$. As time progressively increases, the energy concentrates towards $(k_x = 0, k_y = 1/\sqrt{2})$.

Initially, the response is characterized by an isotropic pattern, reminiscent of the linear growth that is experienced in the first stages of the perturbation growth. As the amplitude becomes sufficiently large, the spectrum shows that the energy is focusing on the axis $k_x = 0$, i.e. streamwise structures are selected. The emergence of streamwise structures agrees well with the results of the fully nonlinear simulation and with the experimental observation. Moreover, the spectrum is localized around $k_y = 1/\sqrt{2}$, the most amplified wavelength predicted by the flat film dispersion relation ((6.3)), and rivulet structures are growing exponentially. Thus, the dynamics of pure streamwise structures stays linear, even in the weakly nonlinear regime.

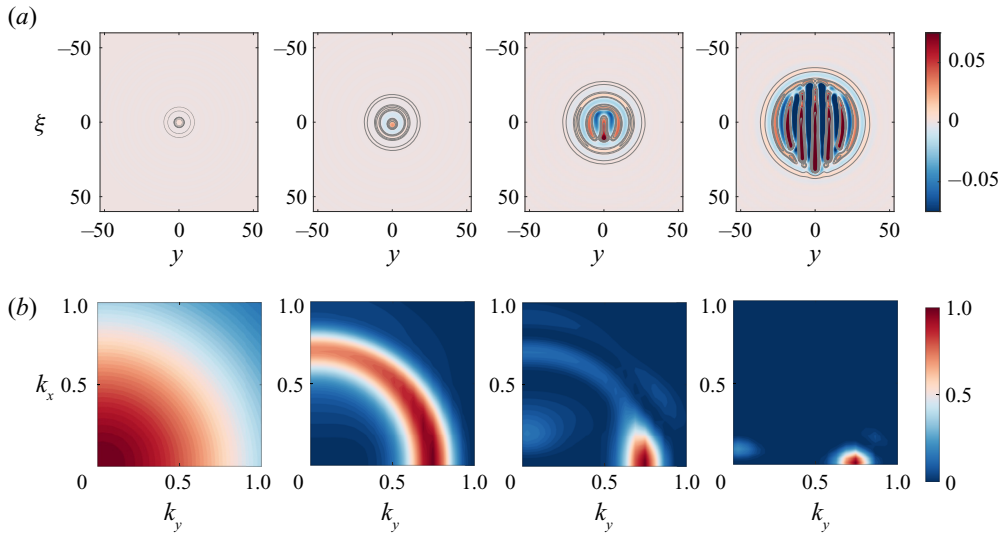


FIGURE 15. Case $u = 5.45$. (a) Impulse response in the moving reference frame ($\xi = x - ut$, y) from the weakly nonlinear model and (b) its two-dimensional Fourier energy spectrum. From left to right: $t = 0$, $t = 30$, $t = 60$, $t = 90$.

The origin of the selection of rivulet structures is identified in the weakly nonlinear advection term $2u\eta\partial_\xi\eta$, which acts in indirect manner to favour rivulet structures while damping all other orientations. The weakly nonlinear model of (6.5) is formally analogous to the linear model of (6.4), except for the weakly nonlinear advection term. It should be noticed that this term influences the dynamics of streamwise-inhomogeneous structures only, on which it is seen to have a damping effect. The nonlinear advection term embodies the difference in the perturbation advection velocity in regions of different thickness and is known to create wave steepening (Babchin *et al.* 1983). The emerging steep gradients are damped by surface tension effects, levelling therefore the non-streamwise structures. In conclusion, the most unstable solution in the weakly nonlinear regime is the one in which the capillary damping is reduced the most, as the term $2u\eta\partial_\xi\eta$, responsible of wave steepening, vanishes.

When only streamwise structures are present, the advection term disappears and the weakly nonlinear model is formally analogous to the linear equation in the moving reference frame (6.4). Consequently, the response of streamwise structures is linear up to second order in the perturbation.

In conclusion, the weakly nonlinear dynamics gives an insight into the origin of the emergence of rivulet structures: the latter are the only ones screened from the action of the difference in the advection. The dynamics of pure streamwise structures remains linear even in the weakly nonlinear regime, thus explaining the agreement between the linear prediction and the experimental measurements at large amplitudes observed in Lerisson *et al.* (2020). At late times, rivulets eventually invade the perturbation region. In the case of steady inlet forcing (figure 2) rivulets invade the whole domain and steady and streamwise saturated rivulet structures emerge downstream, as a result of the weakly nonlinear dynamics. As seen in the previous sections, rivulets may eventually destabilize through a secondary instability, resulting in travelling lenses. In both the emergence and the stability of rivulets, the differences in advection in regions of different thickness is crucial.

7. Conclusions

In this paper, we studied the selection and stability of rivulet structures in a thin film flowing under an inclined planar substrate. When the inlet is steadily forced along the spanwise direction, predominant rivulet structures were experimentally observed, which may destabilize at some distance from the inlet through the development of travelling lenses. Inspired by this experimental observation, we performed a nonlinear simulation with periodic boundary conditions, starting from an initial condition that mimicked the experimental forcing. The response to a streamwise-invariant sinusoidal initial condition confirmed the emergence of a persistent pattern of saturated rivulets, which may destabilize.

We then focused on the study of the mechanisms that may explain the behaviours observed in the experiment and numerical simulations, by studying the secondary stability of one-dimensional and saturated rivulets when perturbed in the streamwise direction. As the relative importance of advection increases, short wavelengths are progressively stabilized and only very large wavelengths remain slightly unstable. We relate their stabilization to the different advection of thickness perturbations on the rivulet profile. An increase in the advection results in steeper gradients for the same perturbation wavelength. Capillary forces counteract the wave steepening and eventually damp the perturbation, for high enough values of the advection. We compared the theoretical results for the spatial amplification of disturbances of the inlet flow rate with extensive experimental measurements of oscillations on rivulets, and confirmed the observation of a steady and saturated rivulet state when high values of u are considered.

Finally, we gave an insight into the early-stage selection of streamwise-aligned structures, as observed in Lerisson *et al.* (2020), by studying the evolution of a localized impulse in the flat film. The experimental response showed that the wavefront selects mostly streamwise structures. The numerical impulse response also showed an initial isotropic growth followed by the selection of predominant rivulet structures. The numerical results were rationalized using a weakly nonlinear model, which showed the same selection of rivulets. The strength of the weakly nonlinear model was to identify one source of nonlinearity as the selection mechanism of streamwise structures, i.e. the weakly nonlinear advection. The latter is known to create wave steepening, counteracted by capillary terms. The evolution leads to levelling of all but streamwise structures. We concluded that the departure from a flat film towards streamwise structures is the solution in which the wave steepening and capillary damping effects are reduced the most. As a consequence, the selection of streamwise structures is due to the difference in the advection of perturbations in regions of different thickness, which acts to level all but pure streamwise perturbations (rivulets), while the dynamics of the latter remains linear even in the weakly nonlinear regime, thus rationalizing the results of Lerisson *et al.* (2020).

Our work aimed at laying rigorous foundations in the study of coating flows on the underside of planar substrates, interpreting the route to dripping as a destabilization of the flat film towards rivulets followed by a secondary instability. Nevertheless, several open questions are left. In complement to the spatio-temporal impulse response studied in this work, the response to a permanent in time but localized in space defect was considered briefly in Lerisson *et al.* (2020). However, a more detailed study to properly quantify the evolution of the response, e.g. in terms of asymptotic properties of the linear response, still needs to be performed.

Despite the predominance of streamwise-oriented structures, for some conditions, lenses appear on rivulets. While in this work a first analysis was performed in terms of spatial growth, a complete analysis of the precise evolution of perturbations along the

streamwise direction remains to be pursued. In particular, a weakly non-parallel approach combined with a global resolvent technique could be suitable in this case. Furthermore, although the rivulet configuration shown in figure 11(b) may seem regular, we sometimes observe catastrophic events: lenses can merge in the streamwise direction, and eventually drip. While this work and the one of Lerisson *et al.* (2020) were focused on the emergence and stability of steady structures, further investigations focused on the dynamics of the travelling lenses are crucial to understand the route to dripping.

Acknowledgements

We acknowledge the anonymous referees for the valuable comments that helped to improve the manuscript. We acknowledge the Swiss National Science Foundation under grant 200021_178971.

Declaration of interests

The authors declare no conflict of interest.

Appendix A. Expression of the Jacobian of the curvature

The operator $\partial_{\tilde{\eta}}\kappa(H)$, in general form, reads

$$\begin{aligned} \partial_{\tilde{\eta}}\kappa(H) = & \frac{(1 + (\partial_y H)^2)\partial_{xx} + (1 + (\partial_x H)^2)\partial_{yy} - 2\partial_x H\partial_y H\partial_{xy}}{(1 + (\partial_x H)^2 + (\partial_y H)^2)^{3/2}} \\ & + \frac{2((\partial_x H)^2\partial_y H - \partial_x H(\partial_y H)^2)}{(1 + (\partial_x H)^2 + (\partial_y H)^2)^{3/2}}\partial_x + \frac{2((\partial_y H)^2\partial_x H - \partial_y H(\partial_x H)^2)}{(1 + (\partial_x H)^2 + (\partial_y H)^2)^{3/2}}\partial_y \\ & - 3\frac{\partial_{xx}H(1 + (\partial_y H)^2) + \partial_{yy}H(1 + (\partial_x H)^2) - 2\partial_x H\partial_y H\partial_{xy}H}{(1 + (\partial_x H)^2 + (\partial_y H)^2)^{5/2}}(\partial_x H\partial_x + \partial_y H\partial_y). \end{aligned} \quad (\text{A } 1)$$

The operator is evaluated for a base flow $H(x, y) = H_r(y)$ (i.e. $\partial_x H = 0$) and we impose $\partial_x \tilde{\eta} = ik_x \tilde{\eta}$.

Appendix B. Absolute-convective transition of the saturated rivulet profile

The purpose of this appendix is to verify the application of the Gaster transformation used in § 4.4. The Gaster transformation is applied in the context of strongly convectively unstable systems.

To verify the convective nature of the instability of the one-dimensional and steady rivulet profile, we evaluate the value of u at which the absolute-convective transition occurs. We thus apply the Briggs–Bers criterion (Briggs 1964; Bers 1975; Huerre & Monkewitz 1990; Schmid *et al.* 2002) to the dispersion relation $D_r(\omega, k_x) = 0$, (4.3). We look for the saddle points in the complex k_x plane $\partial\omega/\partial k_x = 0$ and evaluate the imaginary part of ω at the saddle point $\text{Im}(\omega_0)$. The absolute-convective transition occurs when $\text{Im}(\omega_0) = 0$. A spectral code is implemented in MATLAB, and saddle points are searched for with the built-in function *fsolve*. We identified a single saddle point in the complex- k_x plane. The absolute-convective transition occurs at $u_0 = 0.56$ (figure 16), which is much lower than the values of u used throughout this work. Interestingly, the convective-absolute

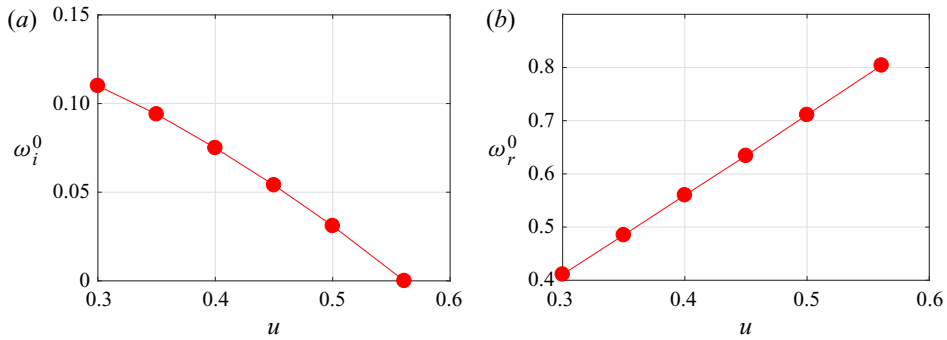


FIGURE 16. (a) Imaginary and (b) real parts of the complex frequency ω_0 for the absolute-convective stability analysis. The absolute-convective transition occurs at $u_0 = 0.56$.

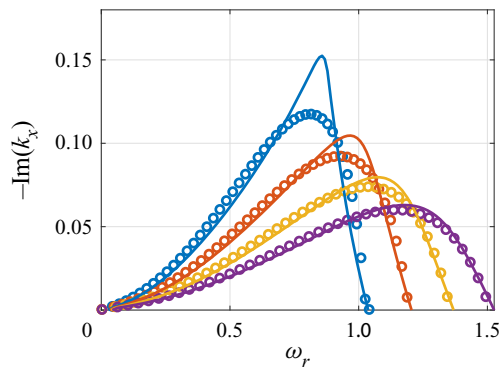


FIGURE 17. Spatial growth rate given by the spatial stability analysis (solid lines) and by the Gaster transformation (circles), for $u = 0.6$ (blue), $u = 0.7$ (orange), $u = 0.8$ (yellow), $u = 0.9$ (purple).

transition for the flat film takes place at $u_0 = 0.54$ (Brun *et al.* 2015), very close to the saturated rivulet value.

In figure 17 we report the comparison between the spatial stability analysis and the Gaster transformation, for $u < 1$. As u approaches the value for the absolute-convective transition, the prediction of the Gaster transformation deviates from the spatial stability analysis results.

REFERENCES

BABCHIN, A. J., FRENKEL, A. L., LEVICH, B. G. & SIVASHINSKY, G. I. 1983 Nonlinear saturation of Rayleigh–Taylor instability in thin films. *Phys. Fluids* **26** (11), 3159–3161.
 BALESTRA, G., KOFMAN, N., BRUN, P.-T., SCHEID, B. & GALLAIRE, F. 2018a Three-dimensional Rayleigh–Taylor instability under a unidirectional curved substrate. *J. Fluid Mech.* **837**, 19–47.
 BALESTRA, G., NGUYEN, D. M.-P. & GALLAIRE, F. 2018b Rayleigh–Taylor instability under a spherical substrate. *Phys. Rev. Fluids* **3** (8), 084005.
 BERS, A. 1975 Linear waves and instabilities. In *Physique des Plasmas* (ed. C DeWitt & J. Peyraud), pp. 117–215. Gordon & Breach.
 BERTAGNI, M. B. & CAMPOREALE, C. 2017 Nonlinear and subharmonic stability analysis in film-driven morphological patterns. *Phys. Rev. E* **96** (5), 053115.

- BRIGGS, R. J. 1964 Electron stream interaction with plasmas. In *Handbook of Plasma Physics* (ed. A. Bers). MIT Press.
- BRUN, P.-T., DAMIANO, A., RIEU, P., BALESTRA, G. & GALLAIRE, F. 2015 Rayleigh–Taylor instability under an inclined plane. *Phys. Fluids* **27** (8), 084107.
- CAMPORALE, C. 2015 Hydrodynamically locked morphogenesis in karst and ice flutings. *J. Fluid Mech.* **778**, 89–119.
- CHANDRASEKHAR, S. 2013 *Hydrodynamic and Hydromagnetic Stability*. Courier Corporation.
- CHAROGIANNIS, A., DENNER, F., VAN WACHEM, B. G. M., KALLIADASIS, S., SCHEID, B. & MARKIDES, C. N. 2018 Experimental investigations of liquid falling films flowing under an inclined planar substrate. *Phys. Rev. Fluids* **3** (11), 114002.
- DUPRAT, C. & STONE, H. A. 2015 *Fluid-Structure Interactions in Low-Reynolds-Number Flows*. Royal Society of Chemistry.
- FERMIGIER, M., LIMAT, L., WESFREID, J. E., BOUDINET, P. & QUILLIET, C. 1992 Two-dimensional patterns in Rayleigh–Taylor instability of a thin layer. *J. Fluid Mech.* **236**, 349–383.
- GALLAIRE, F. & BRUN, P.-T. 2017 Fluid dynamic instabilities: theory and application to pattern forming in complex media. *Phil. Trans. R. Soc. A Math. Phys. Engng Sci.* **375** (2093), 20160155.
- GASTER, M. 1962 A note on the relation between temporally-increasing and spatially-increasing disturbances in hydrodynamic stability. *J. Fluid Mech.* **14** (2), 222–224.
- HUERRE, P. & MONKEWITZ, P. A. 1990 Local and global instabilities in spatially developing flows. *Annu. Rev. Fluid Mech.* **22** (1), 473–537.
- HUERRE, P. & ROSSI, M. 1998 *Hydrodynamic Instabilities in Open Flows*, pp. 81–294. Cambridge University Press.
- KALLIADASIS, S., RUYER-QUIL, C., SCHEID, B. & VELARDE, M. G. (Ed.) 2012 *Falling Liquid Films*. Springer-Verlag.
- KOFMAN, N., ROHLFS, W., GALLAIRE, F., SCHEID, B. & RUYER-QUIL, C. 2018 Prediction of two-dimensional dripping onset of a liquid film under an inclined plane. *Intl J. Multiphase Flow* **104**, 286–293.
- LEE, A., BRUN, P. T., MARTHELOT, J., BALESTRA, G., GALLAIRE, F. & REIS, P. M. 2016 Fabrication of slender elastic shells by the coating of curved surfaces. *Nat. Commun.* **7**, 11155.
- LERISSON, G., LEDDA, P. G., BALESTRA, G. & GALLAIRE, F. 2019 Dripping down the rivulet. *Phys. Rev. Fluids* **4**, 100504.
- LERISSON, G., LEDDA, P. G., BALESTRA, G. & GALLAIRE, F. 2020 Instability of a thin viscous film flowing under an inclined substrate: steady patterns. *J. Fluid Mech.* **898**, A6.
- LISTER, J. R., RALLISON, J. M. & REES, S. J. 2010 The nonlinear dynamics of pendent drops on a thin film coating the underside of a ceiling. *J. Fluid Mech.* **647**, 239–264.
- MARTHELOT, J., STRONG, E. F., REIS, P. M. & BRUN, P.-T. 2018a Designing soft materials with interfacial instabilities in liquid films. *Nat. Commun.* **9** (1), 4477.
- MARTHELOT, J., STRONG, E. F., REIS, P. M. & BRUN, P.-T. 2018b Solid structures generated by capillary instability in thin liquid films. *Phys. Rev. Fluids* **3**, 100506.
- MEAKIN, P. & JAMTVEIT, B. 2010 Geological pattern formation by growth and dissolution in aqueous systems. *Proc. R. Soc. A Math. Phys. Engng Sci.* **466** (2115), 659–694.
- MOISY, F., RABAUD, M. & SALSAC, K. 2009 A synthetic schlieren method for the measurement of the topography of a liquid interface. *Exp. Fluids* **46** (6), 1021.
- RAYLEIGH, LORD 1882 Investigation of the character of the equilibrium of an incompressible heavy fluid of variable density. *Proc. Lond. Math. Soc.* **s1-14**, 170–177.
- RIETZ, M., SCHEID, B., GALLAIRE, F., KOFMAN, N., KNEER, R. & ROHLFS, W. 2017 Dynamics of falling films on the outside of a vertical rotating cylinder: waves, rivulets and dripping transitions. *J. Fluid Mech.* **832**, 189–211.
- ROMAN, B., GAY, C. & CLANET, C. 2020 Pendulum, drops and rods: a physical analogy. [arXiv:2006.02742](https://arxiv.org/abs/2006.02742).
- RUSCHAK, K. J. 1978 Flow of a falling film into a pool. *AIChE J.* **24** (4), 705–709.
- SCHEID, B., KOFMAN, N. & ROHLFS, W. 2016 Critical inclination for absolute/convective instability transition in inverted falling films. *Phys. Fluids* **28** (4), 044107.

- SCHMID, P. J., HENNINGSON, D. S. & JANKOWSKI, D. F. 2002 Stability and transition in shear flows. applied mathematical sciences, vol. 142. *Appl. Mech. Rev.* **55** (3), B57–B59.
- SETTLES, G. S. 2001 *Schlieren and Shadowgraph Techniques: Visualizing Phenomena in Transparent Media*. Springer.
- SHORT, M. B., BAYGENTS, J. C., BECK, J. W., STONE, D. A., TOOMEY III, R. S. & GOLDSTEIN, R. E. 2005 Stalactite growth as a free-boundary problem: a geometric law and its platonic ideal. *Phys. Rev. Lett.* **94** (1), 018501.
- TAYLOR, G. I. 1950 The instability of liquid surfaces when accelerated in a direction perpendicular to their planes. I. *Proc. R. Soc. Lond. A Math. Phys. Sci.* **201** (1065), 192–196.
- WEINSTEIN, S. J. & RUSCHAK, K. J. 2004 Coating flows. *Annu. Rev. Fluid Mech.* **36**, 29–53.
- WILSON, S. D. R. 1982 The drag-out problem in film coating theory. *J. Engng Math.* **16** (3), 209–221.
- YIANTSIOS, S. G. & HIGGINS, B. G. 1989 Rayleigh–Taylor instability in thin viscous films. *Phys. Fluids A Fluid Dyn.* **1** (9), 1484–1501.
- ZACCARIA, D., BIGONI, D., NOSELLI, G. & MISSERONI, D. 2011 Structures buckling under tensile dead load. *Proc. R. Soc. A Math. Phys. Engng Sci.* **467** (2130), 1686–1700.